Aeroacoustic design and characterization of the 3D-printed, open-jet, anechoic wind tunnel of Delft University of Technology

Applied Acoustics 170 (2020) 107504

Contents lists available at ScienceDirect

Applied Acoustics

journal homepage: www.elsevier.com/locate/apacoust

Aeroacoustic design and characterization of the 3D-printed, open-jet, anechoic wind tunnel of Delft University of Technology

Roberto Merino-Martínez [a,*], Alejandro Rubio Carpio [a], Lourenço Tércio Lima Pereira [a], Steve van Herk [b], Francesco Avallone [a], Daniele Ragni [a], Marios Kotsonis [a]

[a] Faculty of Aerospace Engineering, Delft University of Technology, Kluyverweg 1, 2629 HS Delft, The Netherlands
[b] Electronic and Mechanical Support Division, Delft University of Technology, Mekelweg 4, 2628 CD Delft, The Netherlands

ARTICLE INFO

Article history:
Received 5 February 2020
Accepted 19 June 2020
Available online 13 July 2020

2020 MSC:
00-01
99-00

Keywords:
Aeroacoustic wind tunnel
Acoustic characterization
Flow characterization
Microphone array

ABSTRACT

The newly refurbished vertical tunnel (V-tunnel) at Delft University of Technology has been redesigned as a state-of-the-art facility for research in aeroacoustics (A-tunnel), as well as fundamental studies in laminar-turbulent transition and flow control. This manuscript focuses on the design and refurbishment aspects of the facility, including a description of the main modifications in the supporting structures and the drive system of the fan, with details of the flow conditioning and anechoic performance. A rigorous aeroacoustic and aerodynamic characterization of the facility is also presented, benchmarking the flow quality and acoustic performance of the new wind tunnel with respect to other aeroacoustic facilities across the world.

1. Introduction

The interest in aeroacoustic and flow control research has steadily increased in the last decades [1,2]. Motivated by new sustainability regulations that nowadays affect a broad range of fields such as wind energy, ground vehicles and air transport [3], recent research studies have identified the reduction of noise emissions as one of the most important design targets for manufacturers of aircraft [4] and wind turbines [5,6]. Independently of the complexity of the machine, the aeroacoustic sources of noise of a generic mechanical system depend on the interaction of the object geometry with the flow surrounding it. Therefore, in order to reduce the noise levels generated by these sources, fundamental knowledge of the underlying noise generation mechanisms in function of the aerodynamic regimes is required. In a similar manner, understanding, modeling and controlling critical aerodynamic processes, such as laminar-turbulent flow transition or flow separation is pivotal for the development of future low-emission technological solutions. The advances in computational aerodynamics and aeroacoustics [7–9] have greatly contributed to the study of the complex structures responsible for laminar-turbulent transition and noise generation at realistic Reynolds numbers. These studies, however, require support from equivalently accurate experimental validations [10].

Aeroacoustic and aerodynamic experiments are normally performed in field tests or in wind-tunnels measurement campaigns. Whereas full-scale field experiments accurately represent realistic operational conditions in terms of Strouhal and Reynolds numbers [11], they are relatively expensive, as well as challenging in the control of both aerodynamic properties and sound propagation (usually over a relatively large distance) at the same time. Wind tunnels, on the other hand, offer very controlled flow conditions, although at the cost of a necessary down-scaling of the model, which poses additional challenges for scaling of the obtained results [12]. In the wide range of aerodynamic facilities for industrial or academic research studies, two main categories of wind tunnels can be distinguished, each one presenting its own benefits and challenges for an accurate representation of the investigated flow field. Focusing only on the test section and without considering the typology of the wind-tunnel circuit, which can recirculate the flow (i.e. closed circuit or Göttingen type) or provide with fresh new one (i.e. open circuit or Eiffel type), conventional wind tunnels can be built in a:

* Corresponding author.
E-mail address: r.merinomartinez@tudelft.nl (R. Merino-Martínez).

https://doi.org/10.1016/j.apacoust.2020.107504
0003-682X/

- **Closed-section configuration:** a wind tunnel with a confined testing region typically allows for a quicker realignment of the freestream flow, entailing lower corrections for model blockage and circulation with a relatively better-controlled aerodynamic properties. Since in these configurations the wind-tunnel's walls counteract the circulation effect of the lifting models in the flow, these facilities are typically instrumented with wall-pressure ports, able to recover the aerodynamic lift from the pressure imbalance on the confinement region. This greatly reduces the costs associated with instrumentation of the model and provides with a non-intrusive measurement approach of the aerodynamic performance from an indirect effect [13]. For the same purpose, recent studies are focusing on extending the aerodynamic capabilities of closed-section wind tunnels to host acoustic measurements, mainly by installing microphones on the floor, ceiling or surrounding walls flush-mounted [14] or recessed in cavities [15]. However, the amplitude of the pressure fluctuations in the turbulent boundary layer (TBL) developing along the wind-tunnel's walls is typically few orders of magnitude higher with respect to the acoustic signals propagated from the test models installed in the middle of the test section. In addition, typically high background noise levels [16] and reflections from the solid surfaces of the test section can lead to erroneous measurements of the sound levels emitted by the model [17,18].
- **Open-jet configuration:** a wind tunnel with an open jet is characterized by the formation of a jet-shear layer from the nozzle's exit. The exit of the jet in a relatively larger domain allows for reducing the aforementioned wall effects and lowering the background noise levels compared to their closed-sections counterparts. Measurement instrumentation is additionally less intrusive, due to the flow and optical accessibility that the open jet entails, providing spaces for instrumentation, such as microphone arrays, that can be placed outside of the flow. In fact, according to Pereira Gomes [19], achieving reliable absolute sound pressure levels (L_p) in wind-tunnel experiments is only possible when using this type of wind tunnel configuration. On the other side, due to the jet spreading and the model circulation, the flow quality and alignment are generally more difficult to be controlled, and heavy corrections are necessary for obtaining the effective angle of attack and effective aerodynamic coefficients [20]. Acoustic effects such as refraction through the shear layer at the boundary between the open jet and surrounding flow needs also to be accounted for, especially when considering the distortion in phase of signal collected from microphones at a relevant distance from the model [21–23], or when considering spectral broadening due to shear layer turbulence [24,25].

The vast majority of scientific and industrial wind-tunnel facilities are primarily designed for aerodynamic purposes [10] and are therefore, not optimally designed for acoustic measurements. The two main targets for aeroacoustic measurements in a wind tunnel are the abatement of background noise levels and a fully anechoic environment. The former can be achieved by a careful design of the elements within the wind tunnel circuit and the application of noise reduction measures (such as silencers), whereas the latter is usually obtained by covering the walls, floor and ceiling of the room hosting the test section with acoustic absorbing foam to suppress reflections and approximate free-field sound propagation conditions [26].

In the last decades, several aeroacoustic wind tunnels have been developed ranging from relatively small wind tunnels for academic research to large wind tunnels for industrial purposes. Aeroacoustic wind tunnels can be obtained either by adapting existing facilities [27] or by designing completely new facilities from scratch [10,28]. The current work focuses on the aerodynamic and acoustic characterization of the recently refurbished anechoic open-jet wind-tunnel at Delft University of Technology (A-tunnel), which was formerly known as V-tunnel.

The paper is structured as follows. Section 2 briefly describes the wind-tunnel facility and the new acoustic treatment of the test chamber. Explanations of the measurement systems available and used for the characterization, such as a phased microphone array, are provided in Section 3. The characterization of the new wind tunnel is detailed in Sections 4 and 5 for the aerodynamic and acoustic properties, respectively. Lastly, the conclusions are gathered in Section 6.

2. Wind-tunnel facility

The A-tunnel is an open-jet, closed-circuit, vertical wind-tunnel. This facility was used prior to the refurbishment (formerly known as V-tunnel) for airfoil trailing-edge noise studies and for the performance assessment of trailing-edge serrations as a noise reduction measure [5,29]. Additional studies on laminar-turbulent transition and active flow control have been carried out in the same facility [30,2]. The structural circuit of the A-tunnel is part of the building of the Low Speed Laboratory (LSL) of Delft University of Technology, located at Cornelis Drebbelweg 3, Delft. The wind tunnel spans four different floors and it can be divided into four corresponding segments (following the numbering indicated in Fig. 1a):

1. The settling chamber is located on the ground floor, and it consists of a square room with a side of approximately 6.4 m and a height of 5 m. The settling chamber room has two outer walls (north and west), while the south and east walls are internal to the building. As part of the refurbishment, the inner side of all four walls, as well as ceiling and floor, were covered with acoustic and thermal isolation, preventing any reflection in a sound frequency range between 150 Hz to 20 kHz.
2. The contraction shape presents one of the major changes from the original design and it connects the ground to the second floor. It is supported from the sidewalls of the settling chamber via 4 steel structures, accommodating a sliding crane to allow for maintenance and cleaning of the different parts. The contraction part additionally hosts the inlet lip, the flow straightener, anti-turbulence screens and the final converging nozzle leading to the outlet of the wind.
3. The open-jet test section is located inside the anechoic plenum on the second floor, see Fig. 4a. The floor of the anechoic plenum is approximately a square of 6.4 m $\times$ 6.4 m and the height of the room is 3.2 m.
4. The room where the fans and the collector are located is found on the third floor.

The main elements of the A-tunnel are illustrated in Fig. 1b as an artist impression and described in the list below:

- **A** – Ramps with perforated plates, designed to lead the airflow from the engines to the settling chamber, while maintaining a uniform flow distribution. The slope of the plates is approximately 12°. The porosity of the metal plates was chosen based on the mass-flow to be provided to the wind tunnel. By imposing the condition that a uniform transpiration velocity distribution needs to be ensured along the slope, a linear pressure drop can be computed from which the plate porosity can be adapted. The choice of perforated metal plates allows easy removal and maintenance, especially when using seeding particles for Particle Image Velocimetry (PIV).

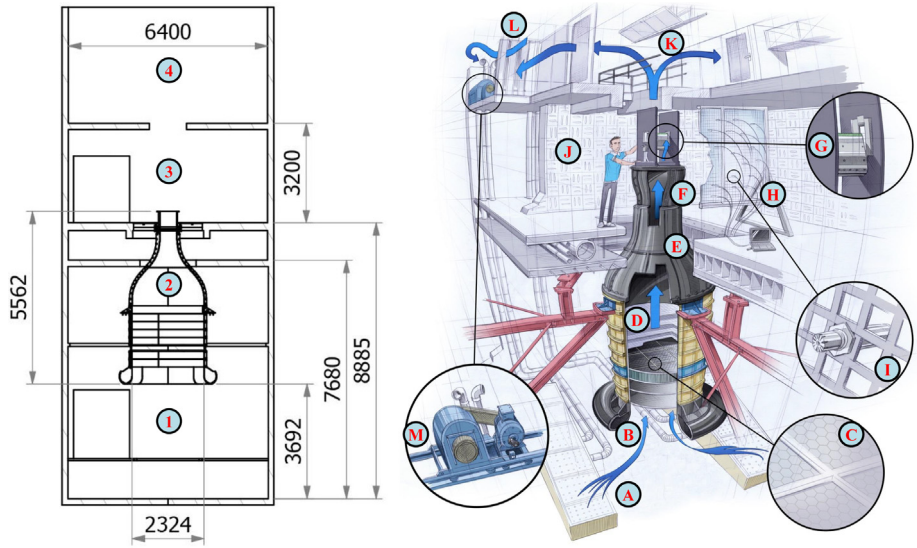

(a) (b)

Fig. 1. (a) Side view of the A-tunnel facility (dimensions are in mm). (b) Artist impression of the A-tunnel facility (illustration by Stephan Timmers).

- **B** – A rounded inlet to the contraction was computationally designed in order to ensure smooth inlet conditions and avoid flow separation in the full regime. The lip was designed as a 2:1 ratio ellipse and constructed in three segments which were 3D-printed (see below for additional details). To further ensure minimal flow separation, the inlet is furbished with a coarse screen mesh of approximately 57% open area, providing a mild pressure jump to stabilize the flow.
- **C** – Following the inlet, the airflow is conditioned using a honeycomb flow straightener. The flow straightener is custom made using corrugated stainless steel of 0.127 mm thickness. The hexagonal cell size is 9.5 mm. The open area coefficient is approximately 94%. The stream-wise length of the flow straightener is 140 mm. Due to the vertical orientation of the wind tunnel, a critical point to the design of the flow straightener was the minimization of downward bending due to its own weight. This was reduced to less than 1 mm using a reinforcement of the honeycomb structure with thin transverse stiffening steel plates arranged in a rectangular pattern.
- **D** – Downstream of the flow straightener, four anti-turbulence screens are arranged at an interval distance of 200 mm. The screens are made of rectangular stainless steel meshes of diameter 0.25 mm and with a cell size of 1 mm arriving at an open area coefficient of 64.5%. The four screens are pre-tensioned and installed on removable wooden rings, facilitating periodic maintenance and cleaning, see Fig. 2.
- **E** – The converging channel was designed using the guidelines by Morel [31] and validated using CFD in order to ensure minimal flow separation and high flow uniformity. The final channel was constructed in four double curvature segments using large-scale 3D-printing. The segments were assembled, welded and hand polished in-situ, see Fig. 2. It is noteworthy to mention that the convergent channel of the A-tunnel possibly represents the first and largest to date component of its kind, solely fabricated using 3D-printing. The intake diameter of the channel is 2.324 m, while the outlet retained at the original V-tunnel diameter of 0.6 m, arriving at an overall contraction ratio of 15. The height of the converging channel is 3.83 m (spanning through the first floor, see Fig. 1a).

Fig. 2. Detail of the A-tunnel contraction and flow conditioners inside it.

- **F** – Outlet nozzle of the wind tunnel. The design of the A-tunnel allows for the use of interchangeable nozzles that can be flush-mounted to the exit of the contraction. There are currently five different nozzles available, intended for achieving different flow conditions. Fig. 3 and Table 1 summarize the main characteristics of the nozzles, i.e. the dimensions of the inner contour and the height of the nozzle's exit, contraction ratio (ratio between the area of the contraction's intake divided by the area of the nozzle's exit), and the maximum flow velocity.
- **G** – Example of a test airfoil mounted between the support side plates. A mechanical system is available for changing the angle of attack automatically.
- **H** – Microphone array for acoustic imaging. See more details in Section 3.3.
- **I** – Detail of the placement of a microphone in the array structure, see 3.3 for more information.
- **J** – Anechoic plenum around the test section. The walls and ceiling of the anechoic room were covered with wedges made of Flamex acoustic absorbing foam [32], see Fig. 4a, in order to avoid unwanted sound reflections. The dimensions of the foam wedge geometry employed are observed in Fig. 4b. A common

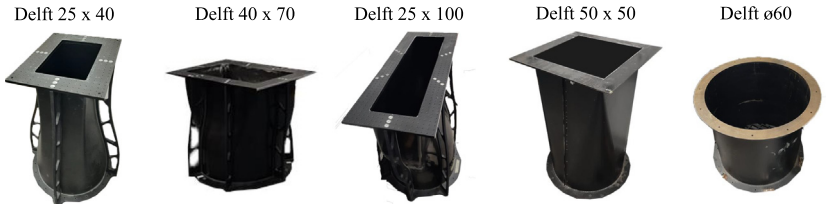

Fig. 3. Photographs of the nozzles from Table 1.

Table 1
Geometry and characteristics of the different nozzles and their exit plane available in the A-tunnel.

Name	Dimensions [m]	Height [m]	Contraction ratio	V_{max} [m/s]
Delft 25 × 40	0.25 × 0.4	1	42:1	74
Delft 40 × 70	0.4 × 0.7	0.72	15:1	35
Delft 25 × 100	0.25 × 1	1	17:1	40
Delft 50 × 50	0.5 × 0.5	1	17:1	38.8
Delft ϕ60	Diameter 0.6	0.6	15:1	35

criterion to determine the geometry of the acoustic foam wedges is that the total height of the wedge should be larger or equal than a quarter of the acoustic wavelength ($\lambda/4$) of the design frequency cutoff [33]. The selected wedge geometry (with a total height of 0.49 m) should allow for free-field propagation of sound for frequencies above approximately 173.5 Hz. The floor was covered by the same type of acoustic absorbing foam with an additional metal grid on top of it with square grid holes of 10 mm side. The grid allows access to the wind-tunnel facility and the transport of measurement equipment, while not generating unwanted sound reflections within the frequency range of interest. Section 5.2 below assesses the free-field sound propagation conditions of the anechoic plenum.

- **K** – Collector covered with acoustic absorbing foam that splits the flow towards the return leg of the A-tunnel.
- **L** – Splitter silencers for absorbing the background noise. There are two sets of silencers on each side of the fan room (pointed by the two diverging blue arrows on the top of Fig. 1b. Each set of silencers consists of three blocks of acoustic absorbing foam of 0.2 m width, 2.5 m length and 2.6 m height. These blocks have a separation between each other of 0.1 m. The inner walls of the airline in this section are also covered with acoustic absorbing foam, ensuring maximum sound absorption in the frequency range of interest.
- **M** – Detail of one of the two engines and fans driving the A-tunnel. The flow is accelerated through the contraction by a pressure difference generated by two *Ferrari* industrial centrifugal fans from the collector to the contraction nozzle. The fans provide a maximum volumetric air flow per fan of approximately 13,500 m^3/h and a maximum static pressure discharge of approximately 9000 Pa. Each fan has ten rotor blades and an installed power of 30 kW. Thus, at the maximum rotational speed (about 3000 rpm), the expected blade passing frequency (BPF) is approximately 500 Hz. This tonal component is normally the dominant noise signature on typical wind-tunnel fans, but it is not perceived at the test section, see Section 5.1.

Besides the acoustic treatments aforementioned, several layers of sound absorbing materials were added in the inner part of the piping system connecting the room of the fans with the ground floor, as well as in the collector region.

The conversion of the previous wind-tunnel facility (known as V-tunnel) to an aeroacoustic wind tunnel was a long process that consisted of three main consecutive upgrades:

1. Installation of the new 3D-printed contraction, see Figs. 1 and 2, and construction of the anechoic plenum around the test section by covering walls, ceiling and floor with wedges made of Flamex acoustic absorbing foam [32], see Fig. 4a.
2. Replacement of the existing fan system by two centrifugal fans in the room at the third floor and removal of the older wind-tunnel control cabinet from the anechoic plenum.
3. Refurbishment of the fan room (items K and L in Fig. 1b) with acoustic absorbing foam panels and change of the microphone array data acquisition system's controller to a more silent device.

3. Experimental setup

3.1. Pitot tube setup

The mean streamwise velocity at the exit of the nozzle was characterized with a Pitot-static tube, shown in Fig. 5a. The *X*–*Y*–*Z* coordinate system employed for the analysis is also depicted, which has its origin located at the center of the rectangular exit of the cross section, the *X* axis in the streamwise direction, and the *Y* and *Z* axes are parallel to the longest and shortest sides of the nozzle, respectively. The Pitot tube was placed along the *X* axis using a bubble level. Its static and total pressure taps were connected to a *Mensor DPG 2400* pressure gauge, with a measurement range going from −1 kPa to 6 kPa. A total of 200 data samples are averaged for each point recorded at a sampling rate of 15 Hz. The accuracy of the instrument used is of 0.03% of the read value. This setup is used to assess the uniformity of the flow across the test section (see Section 4.1) by measuring the mean streamwise velocity *V* within a *Y*–*Z* cross-plane located 80 mm away from the nozzle exit (*X* = 80 mm). For the case of the Delft 40 × 70 nozzle, the target area comprises a rectangle of 320 mm × 500 mm, see Fig. 5b. The velocity field is characterized every 40 mm and 50 mm in the *Y* and *Z* directions, respectively, i.e. at 99 different points. Five different freestream velocities V_∞ defined as the flow velocity measured with the Pitot tube at (X, Y, Z) = (0 m, 0 m, 0 m) were considered: 15, 20, 25, 30 and 34 m/s.

3.2. Hot wire anemometry (HWA) setup

Hot-wire-anemometry (HWA) measurements were performed with a single-wire *Dantec Dynamics* 55P11 probe (platinum-plated tungsten wire with 5 µm diameter and 1.25 mm length) set parallel to the *Y*-axis. The probe was connected to a *TSI IFA-300* constant-temperature anemometry (CTA) system. The analog

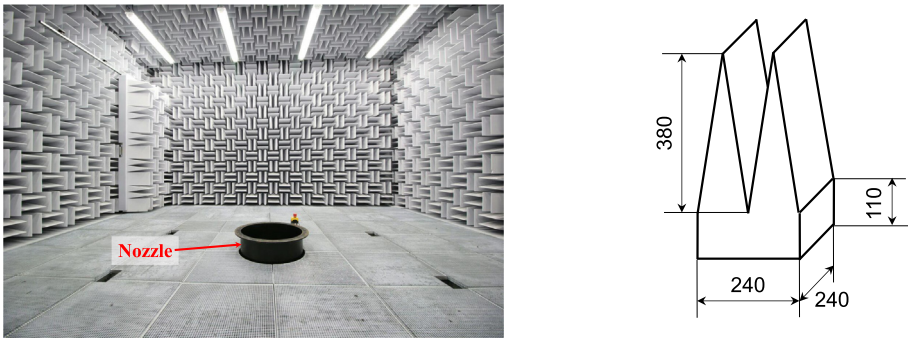

(a) (b)

Fig. 4. (a) Picture of the anechoic plenum of the A-tunnel. (b) Foam wedge geometry (dimensions are in mm).

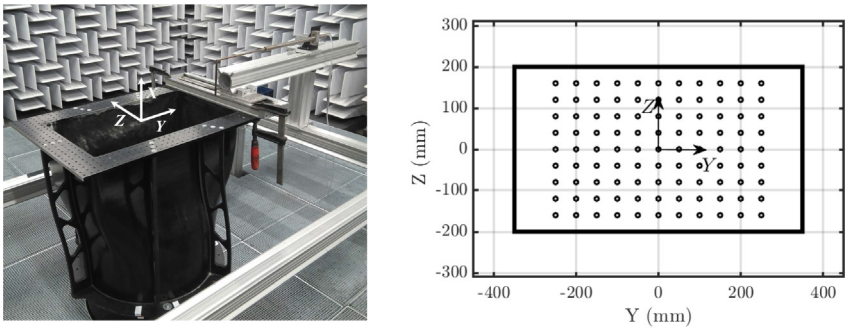

(a) (b)

Fig. 5. Experimental setup for the characterization of the flow field across the test section of the Delft 40 × 70 nozzle: (a) Pitot tube measurements. (b) Locations where Pitot-tube measurements were performed. The inner contour of the nozzle's exit is denoted as a black solid line.

output voltage signal was sampled at 51.2 kHz during 10 s. The calibration was performed employing the previously-described Pitot tube as reference. The relation between the output voltage and the flow velocity was approximated using a fourth-order polynomial fit. Calibration and measurements were completed within 4-hour time windows. In order to correct for any potential deviation from calibration conditions, flow temperature and ambient pressure were also recorded for each measurement. The turbulence intensity of the flow $\sqrt{\overline{v^2}}/V$, where V indicates the mean streamwise velocity and v the streamwise velocity fluctuations, was characterized at the exit of every nozzle. Measurement locations are plotted in Fig. 6(a–e), and the exact coordinates are specified in Table 2. The acquired hot-wire signals were filtered *a posteriori* using a digital band-pass Butterworth filter of third order considering three different frequency bands f_{bp}: 5 Hz to 20 kHz, 20 Hz to 20 kHz, and 40 Hz to 20 kHz.

3.3. Phased microphone array

An acoustic array consisting of 64 *G.R.A.S. 40PH* analog free-field microphones [34] with integrated constant current power (CCP) amplifiers was installed inside of the anechoic plenum of the wind-tunnel. Each microphone has a diameter of 7 mm and a length of 59.1 mm. All the microphones were calibrated individually using a *G.R.A.S. 42AA* pistonphone [35]. The transducers, have flat frequency response within ±1 dB from 50 Hz to 5 kHz and within ±2 dB from 5 to 20 kHz. The data acquisition system (DAS) consisted of 4 *National Instruments* (NI) *PXIe-4499* sound and vibration modules with 24 bits resolution and 204.8 kHz maximum sampling rate. The boards are controlled by a NI *RMC-8354* computer via a NI *PXIe-8370* board. Each microphone is connected to the DAS via a 10-m long *G.R.A.S. AA0028* SMB-BNC coaxial cable [36].

The design and construction of the structure of the phased microphone array were mostly performed during the MSc thesis work of Vlemmix [37]. After considering different design options for the support structure, a trade-off solution was chosen. It was decided to employ three steel perforated plates with square holes in a regular grid pattern to fit the microphones, see Fig. 7a. Each plate has a dimensions of 1 m × 2 m and has a total of 8450 perforations, i.e. possible microphone positions. This design offers a compromise solution between reduced acoustic reflections, robustness and a large number of potential microphone positions.

The default microphone distribution for airfoil-noise measurements corresponds to an optimized multi-arm spiral arrangement [38], with 7 spiral arms of 9 microphones each and an additional microphone located at the center of the array, see Fig. 7b. The dimensions of this array design are approximately 2 m in the X direction and 1 m in the Z direction. The coordinates of the center microphone in the reference system defined in Fig. 5 are $(X, Y, Z) = (0.5, h, 0)$ m, where h is the distance of the array plane to the axis jet. For most experiments, 1 m $\leqslant h \leqslant$ 1.5 m to avoid contact with the shear layer. Different optimized microphone distributions have been used and compared in previous studies [38].

The size of the perforated holes in the steel plates is 10 mm × 10 mm and the thickness of the metallic border to the next hole is 4 mm. This provides an open area ratio of approximately 51%. Two structure configurations are available, featuring two or three

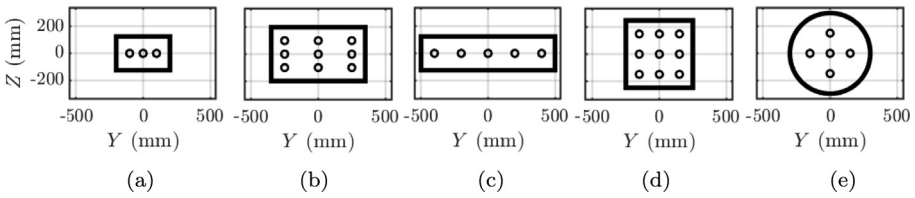

Fig. 6. Turbulence characterization at the nozzles' exit cross-section. Locations where HWA measurements were performed are marked with circles. (a) Delft 25 × 40. (b) Delft 40 × 70. (c) Delft 25 × 100. (d) Delft 50 × 50. (e) Delft ϕ60. The inner contour of the nozzles' exit is depicted as a black solid line.

Table 2
HWA measurement locations (in mm) at each nozzle.

Nozzle		P1	P2	P3	P4	P5	P6	P7	P8	P9
Delft 25 × 40	*Y*	100	0	−100	–	–	–	–	–	–
	Z	0	0	0	–	–	–	–	–	–
Delft 40 × 70	*Y*	250	250	250	0	0	0	−250	−250	−250
	Z	100	0	−100	100	0	−100	100	0	−100
Delft 25 × 100	*Y*	400	200	0	−200	−400	–	–	–	–
	Z	0	0	0	0	0	–	–	–	–
Delft 50 × 50	*Y*	150	150	150	0	0	0	−150	−150	−150
	Z	150	0	−150	150	0	−150	150	0	−150
Delft ϕ60	*Y*	150	0	0	0	−150	–	–	–	–
	Z	0	150	0	−150	0	–	–	–	–

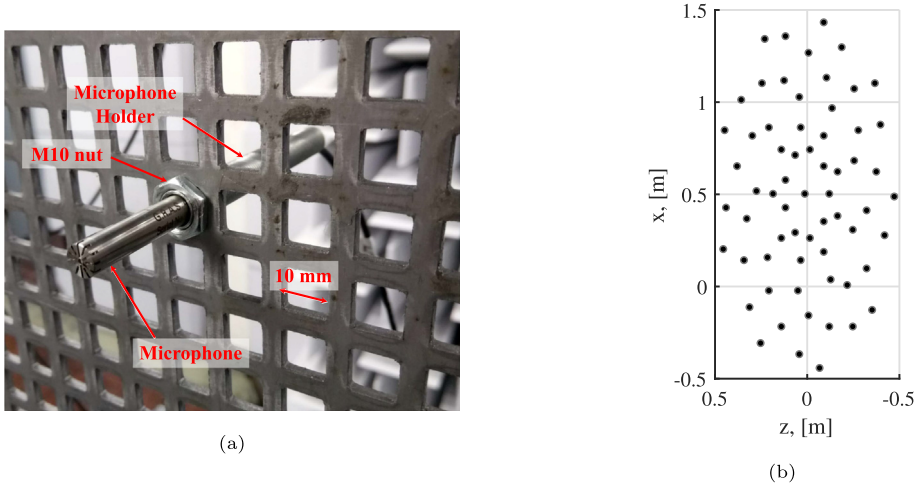

Fig. 7. (a) Detail of the microphone holding system and the perforated plate. (b) Default microphone array distribution for airfoil-noise measurements, as seen from behind.

steel plates, i.e. with total sizes of 2 m × 2 m or 3 m × 2 m. For the experiments performed so far, the configuration with only two plates has been used. Each microphone is placed inside of a holder consisting of a hollow threaded metal rod with an outer diameter of 10 mm and an inner diameter of 8 mm, see Fig. 7a. Thus, there is a perfect fit between the holder's outer diameter and the side of the metallic grid square hole and just 1 mm of margin to insert the microphone inside the holder. The holders can be tightly mounted to the array using two M10 nuts, see Fig. 7a.

All the plates are mounted on a rectangular frame structure manufactured in steel and lifted from the ground using steel legs, see Fig. 8, in a way that the center microphone is aligned with the model to be tested. All the borders of the metallic frame are covered with Flamex acoustic absorbing foam [32] to minimize acoustic reflections [37], see Fig. 8a. The whole structure of the array can easily be moved within the anechoic plenum of the A-tunnel, in case different angles of emission are of interest. Additional details about the support structure can be found in [37].

4. Flow characterization

4.1. Mean flow uniformity

The uniformity of the flow across the cross section of the nozzles' exit plane is investigated in this section. Fig. 9 shows the relative variation of the local mean velocity V with respect to the freestream velocity V_∞ (measured at the center of the nozzle with the Pitot tube, i.e. at $(X, Y, Z) = (0\text{ m}, 0\text{ m}, 0\text{ m})$) for the Delft 40 × 70 nozzle for freestream velocities of 15 m/s (Fig. 9 and 34 m/s (Fig. 9b). Measurement locations are represented in Fig. 9 as circles and the rest of the map levels were computed by linear interpolation using adjacent data. The mean streamwise velocity is found to be uniform within 0.6% for most of the cross section independently

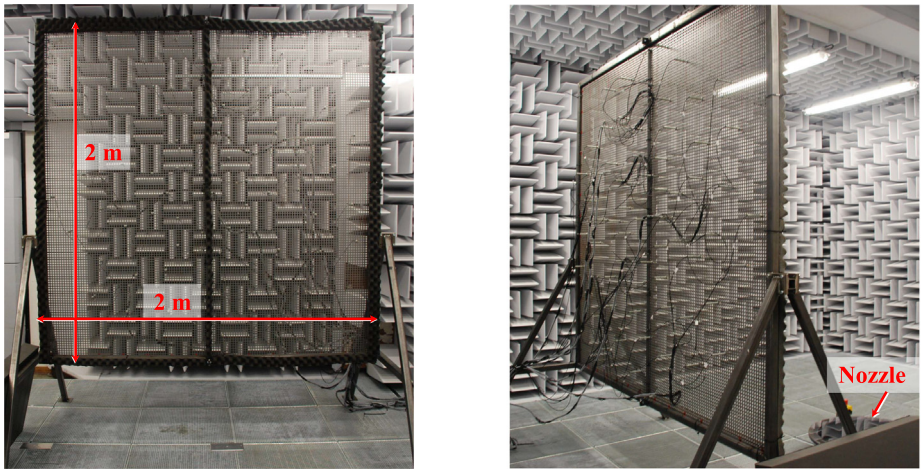

Fig. 8. Pictures of the microphone array structure setup (a) Front view. (b) Back view.

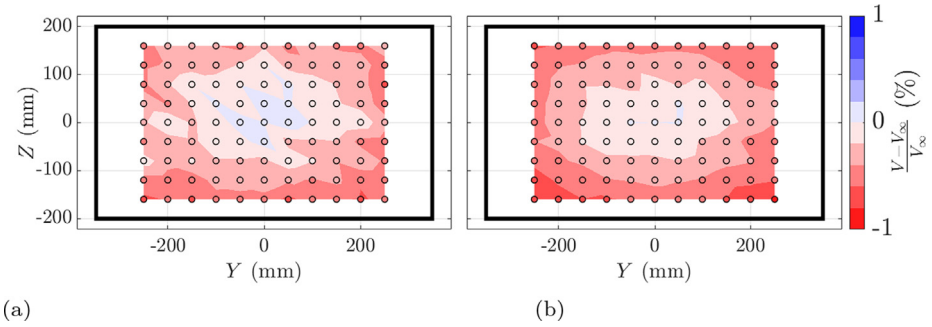

Fig. 9. Mean velocity uniformity $\frac{V-V_\infty}{V_\infty}$ (in %) of the Delft 40 × 70 nozzle. The inner contour of the nozzle exit is represented by the black solid line. (a) V_∞ = 15 m/s. (b) V_∞ = 34 m/s.

of the freestream velocity. Points measured closer to the wall (at Z = ± 100 mm) have a slightly higher velocity deficit with respect to the center of the nozzle; yet, for that region the flow uniformity ranges between −0.6% and −0.8%, which is considered satisfactory. Although not shown here for the sake of conciseness, similar conclusions are drawn from measurements featuring the other nozzles and performed at V_∞ = 20, 25 and 30 m/s.

4.2. Flow turbulence intensity

Streamwise velocity turbulence intensity $\sqrt{\overline{v^2}}/V$ values measured at the center of each nozzle's exit are plotted as a function of the mean streamwise velocity V in Figs. 10(a–e). Here the mean streamwise velocity V is calculated using the HWA data. Data band-pass filtered within $f_{bp} \in [5, 20,000]$ Hz are analyzed in the following. Data measured for the Delft ϕ60 nozzle (Fig. 10(e)) shows lower turbulence intensity levels: at V = 2.5 m/s, the turbulence intensity is 0.14%; above 10 m/s, $\sqrt{\overline{v^2}}/V$ decreases below 0.1% up to 0.06% at 34 m/s. For the present nozzle, increasing the filter's lower bound to 20 Hz or 40 Hz does not yield relevant changes in turbulence intensity at any speed, which indicates that the kinetic energy content within 5 Hz and 40 Hz is, thus, negligible compared to the overall energy contained in the signal. For the rest of the nozzles (Fig. 10(a–d)), similar turbulence intensity levels (below 0.1%) are found for $V \geqslant 10$ m/s. Below that mean velocity, turbulence intensity values are higher (up to 0.1% higher for the Delft 40 × 70 nozzle) than those reported for the Delft ϕ60 nozzle (for equivalent speeds). Increasing the lower frequency bound of the band-pass filter to 20 Hz decreases the turbulence intensity slightly (with reductions up to 0.02% depending of freestream velocity) for all the rectangular/squared nozzles. It is interesting to note that the $\sqrt{\overline{v^2}}/V$ values on signals filtered within 20 Hz and 20 kHz are similar independently of the nozzle; such a rapid change of shape (from round at the contraction level to squared/rectangular at the outlet cross-section) only produces additional fluctuations within 5 Hz and 20 Hz. Further raising the filter's low-frequency bound to 40 Hz does not entail any additional decrease of turbulence intensity. Overall, the turbulence intensity is below 0.22% independently of the nozzle or freestream velocity. This result is in line with other open-jet facilities [10,28,39–42], and it can be, therefore, considered satisfactory.

4.3. Spectral density of the velocity fluctuations

The spectral content of the velocity fluctuations measured with HWA is analysed in the following. The power spectral density (PSD) of the velocity fluctuations Φ_{vv} is plotted in Fig. 11a and b for the Delft 40 × 70 nozzle and the Delft ϕ60 nozzle, respectively. For the sake of clarity, only measurements at 10, 20 and 30 m/s are shown. The data measured with the fans off (V = 0 m/s) are also reported for completeness. Spectral peaks are measured at 150, 250, 350,..., 4450 Hz independently of nozzle type or freestream velocity. Since such phenomena are also present in data measured at 0 m/s, it can be concluded that

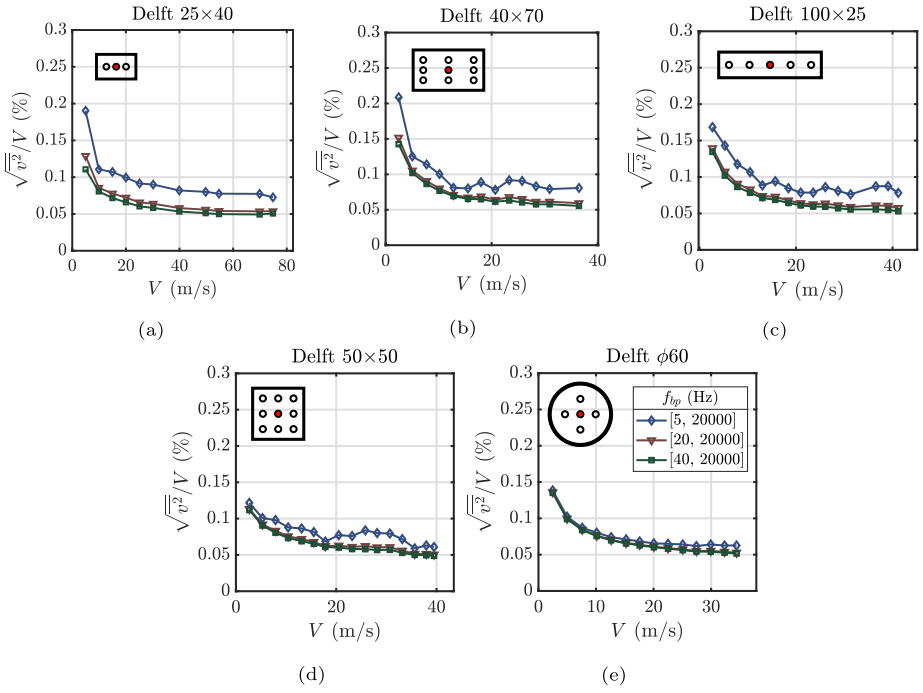

Fig. 10. Streamwise turbulence intensity $\sqrt{\overline{v^2}}/V$ as a function of the mean streamwise velocity V at the centroid of each nozzle's exit. Acquired signals are band-pass filtered within the frequency range f_{bp}, specified in the legend. (a) Delft 25 × 40. (b) Delft 40 × 70. (c) Delft 25 × 100. (d) Delft 50 × 50. (e) Delft ϕ60.

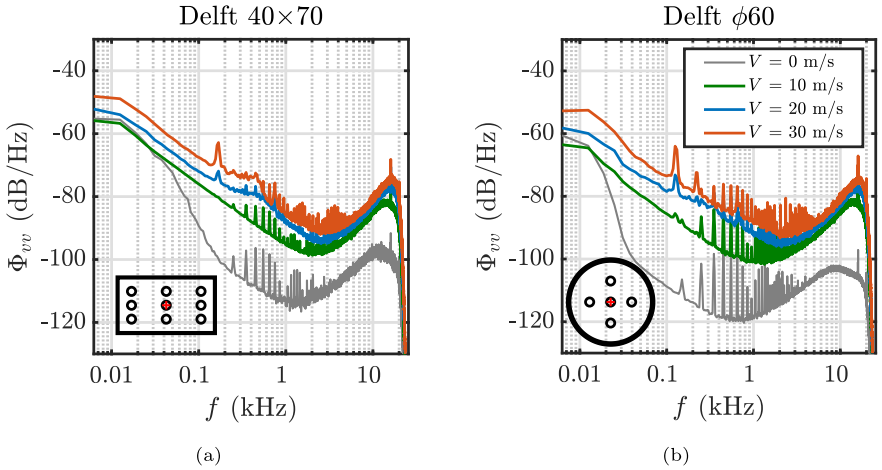

Fig. 11. Spectral density of the velocity fluctuations Φ_{vv} at the center of the nozzle's outlet cross-section for mean streamwise velocities V of 10, 20 and 30 m/s. (a) Delft 40 × 70. (b) Delft ϕ60.

they are caused by electronic noise within the data acquisition system. A similar conclusion can be drawn for the peak reported at 16 kHz. It is also interesting to note that below certain frequencies (25 Hz in Fig. 11a; 12.5 Hz in Fig. 11b), data measured at 0 m/s contain similar or even higher energy than those measured at 10 m/s. This can be attributed to the presence of residual circulation of airflow through the wind tunnel. Finally, spectral peaks are also reported at 168.8 Hz (Fig. 11a) and 125 Hz (Fig. 11b). It is observed that the peaks do not change in frequency with the mean flow velocity V, and only their magnitude is increased. This is attributed to the standing wave created by the jet column. In fact, the indicated frequency scales with the distance between the jet and the collector because of the different heights of the nozzles, see Table 1.

5. Acoustic characterization

For the acoustic characterization of the A-tunnel, the aforementioned microphone array (see Section 3.3) was employed. For all the measurements explained in this section, a recording time of 30 s and a sampling frequency of 51.2 kHz were used. The frequency spectra of the different sound signals were obtained with the Welch's method [43,44] using a block length of 8192 samples (0.16 s), a Hanning windowing function and 50% data overlap (and therefore a 8/3 correction factor), providing a frequency resolution Δf of 6.25 Hz. The frequency range of analysis for the characterization of the facility extends from 20 Hz to 20 kHz, because it is the relevant frequency range for the human ear [45] and due to the characteristics of the microphones used [34]. This frequency range contains the frequencies of interest for typical aeroacoustic

measurements in the A-tunnel which, given the usual downscaling of the test model, require the study of the noise emissions at high frequencies.

5.1. Background noise measurements

The background noise inside of a wind-tunnel facility is mostly caused by the fan, the flow noise from the jet (which scales with the 8th power of the flow velocity [46] and can be considered as the physical lower limit of the background noise), and the interaction of the jet with the collector [10]. Due to the success of noise-reduction measures, the airframe noise signals to be measured are becoming closer to the background noise levels of the wind-tunnel facilities [47]. For example, some test models can be inherently very quiet, such as airfoils equipped with trailing-edge serrations [5,29] or permeable inserts [48]. Therefore, it is essential to achieve background noise levels as low as possible. Ideally, a signal to noise ratio of at least 10 dB between the sound signal to be measured and the background noise is desired [10].

The background noise levels of the A-tunnel facility for different flow speeds (in steps of 2.5 m/s) were recorded by the microphone array, which was located at a distance of 1 m from the center of the jet. This process was repeated for each of the five nozzles, employing a microphone aligned with the nozzle's exit and perpendicular to the jet axis. Therefore, the emission angle with respect to the normal direction of the nozzle's exit plane θ considered was 90°, where $\theta = 0°$ corresponds to the streamwise direction. Fig. 12 depicts the (a) narrowband and (b) one-third-octave band background noise spectra for different flow velocities (including 0 m/s) for the Delft 40×70 nozzle. As expected, the background noise levels increase with the flow velocity. The narrowband spectrum for the flow velocity of 10 m/s presents a tone at a frequency of 890 Hz that protrudes about 8 dB with respect to the surrounding broadband noise. This tone is also present at the same velocity for the other nozzles, but not at higher velocities. Applying acoustic imaging to the data recorded by the microphone array determined that the source for this tonal noise is located near the collector and the fan room. A smaller peak at 325 Hz was detected for higher velocities, the source of which is also located on the upper floor. Both sound sources are located considerably far away from the focus direction of the array and are, therefore, not expected to interfere with the acoustic measurements performed in the test section using acoustic imaging techniques. In the one-third-octave band spectra (Fig. 12b), the aforementioned peaks at 325 Hz and 890 Hz are not visible, but a small hump is noticeable at the band centered at 63 Hz, most likely due to electric noise (also known as mains hum). The exact cause of this hump remains unknown, since the spatial resolution of the microphone array is insufficient for such a low frequency. However, this frequency is very low and outside of the frequency range of interest for typical experiments in this facility. Similar spectra was obtained for the rest of the nozzles, with minor differences. The background noise spectra without flow with the driver system on and off were virtually the same, i.e. turning on the driver system did not cause a measurable increase in the background noise levels.

The overall L_p background noise values and the A-weighted noise levels ($L_{p,A}$) for the Delft 40×70 over a frequency range between 20 Hz and 20 kHz are plotted with respect to the flow velocity V_∞ in Fig. 13a. The case with A-weighting is considered,

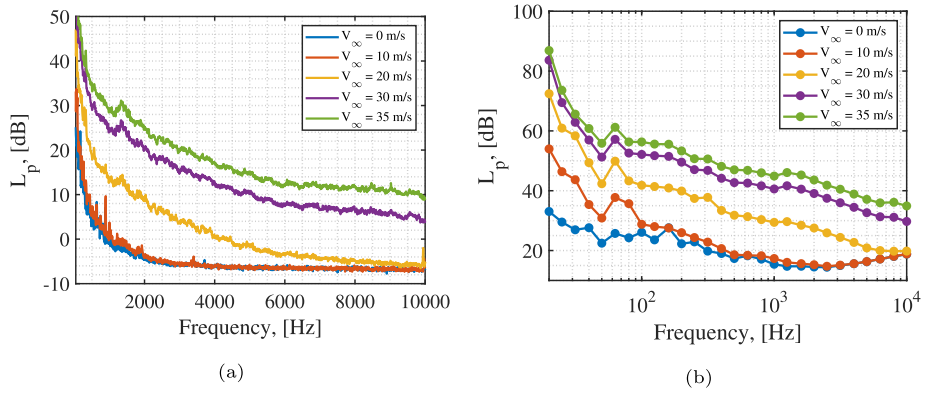

Fig. 12. Background noise spectra for different flow velocities V for the Delft 40×70 nozzle: (a) narrowband ($\Delta f = 6.25$ Hz) and (b) one-third-octave bands (note the logarithmic scale in the X axis).

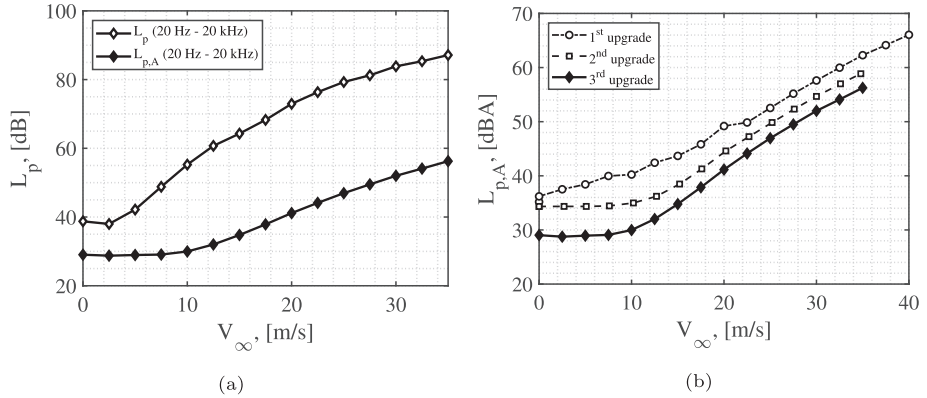

Fig. 13. (a) Overall L_p and $L_{p,A}$ background noise levels for different flow velocities for the Delft 40×70 nozzle. (b) Overall $L_{p,A}$ background noise levels for the same nozzle after the three consecutive upgrades of the A-tunnel.

since that condition is usually employed for comparing background noise levels between different wind tunnels [10,16,28]. It is observed that applying A-weighting considerably reduces the noise levels (up to 30 dB for the higher velocities considered), indicating the strong low-frequency noise content of the signal (see Fig. 12) since this procedure considerably reduces the contribution of that part of the spectrum.

For illustrative purposes, the A-weighted overall background noise levels with respect to the flow velocity after the three upgrades applied to the A-tunnel mentioned at the end of Section 2 are depicted in Fig. 13b. In general, reductions of up to 10 dBA have been achieved with the third and final upgrade with respect to the first upgrade.

The overall A-weighted background noise levels ($L_{p,A}$) of aeroacoustic wind tunnels are normally compared with those from other similar facilities by employing a scaling formula [10], which takes into account the different exit area of the nozzle, S_{nozzle}, and the distance between the observer and the axis of the jet, r:

$$L_{p,A,norm} = L_{p,A} - 10\log\left(\frac{S_{nozzle}}{r^2}\right), \quad (1)$$

where $L_{p,A,norm}$ is the normalized A-weighted background noise level. In such a way, the noise levels are normalized to a nozzle with an exit area of 1 m^2 and an observer located 1 m away from the jet axis.

The first comparison of the $L_{p,A,norm}$ values corresponds to the five nozzles available at the A-tunnel, see Fig. 14. The characteristics of these nozzles are presented in Tables 1 and 3. It is observed that the scaled background noise levels of the five nozzles follow a similar trend and collapse in a satisfactory way for most of the velocity range. The A-weighted background noise levels (without applying the normalization of Eq. (1)) for each nozzle at a flow velocity of 30 m/s are also included in Table 3 for comparison purposes.

One consideration when studying background noise levels of wind tunnels is their dependence with the flow velocity. It is expected that higher flow velocities imply higher background noise levels, usually following a power law with respect to velocity with exponent k, such as

$$L_{p,A,V} - L_{p,A,V_{ref}} = 10k\log\left(\frac{V}{V_{ref}}\right), \quad (2)$$

where $L_{p,A,V}$ is the A-weighted background noise level at a velocity V and $L_{p,A,V_{ref}}$ is the A-weighted background noise level at a reference velocity V_{ref}. The values of k in this paper are obtained using a least-squares fit.

Ideally, the exponent k should be as close as possible to a value of 8, since that would mean that the main noise source in the wind tunnel is the jet noise coming from the nozzle [10], rather than other sources of mechanical noise or fluid-solid interaction noise, which typically scale with a lower exponent value [47]. The exponent values for the five nozzles of the A-tunnel are listed in the last column of Table 3 and have values between 6.2 and 6.9. The 6th and 7th power laws have been plotted in Fig. 14. It seems that, as the flow velocity increases (especially after 40 m/s), the behaviour of the background noise levels changes from $k \approx 6$ to $k \approx 7$. The nozzle Delft 25 × 40 presents the highest exponent value. These values are similar to those of other aeroacoustic wind-tunnel facilities [10,16,28], see Table 4.

An extensive comparison of the background noise levels of the A-tunnel with other existing open-jet aeroacoustic wind tunnels from the literature was performed. The comparison was divided in two categories: small wind tunnels of universities or research institutions, see Fig. 15a, and large industrial facilities, mostly from the automotive industry, see Fig. 15b. Table 4 contains the details of the nozzles of each wind tunnel compared. For clarity reasons, only the results of two nozzles from the A-tunnel are shown in the comparisons: Delft 25 × 40 and Delft 40 × 70. These two nozzles have been the most used for aeroacoustic experiments so far.

All the background noise levels of other wind tunnels were scaled using Eq. (1) on the values found in literature [10,16,28,40,49–55]. Despite this normalization, it is quite likely that different wind-tunnel facilities used different ways to measure and process the acoustic data, thus, the results presented in this comparison should only be considered as indicative. The characteristics about the exit area of the nozzles, the maximum flow velocity V_{max}, the emission angle considered θ with respect to the normal direction of the nozzle's exit plane, and the exponent of the power law k are presented in Table 4. It should be noted that lower values of θ imply that the microphone location was made further downstream, i.e. at a larger streamwise direction from the nozzle's exit plane.

The universities and research institutions considered for comparison were (in alphabetic order): the University of Adelaide in Autralia, Beihang University in China [52], the University of Bristol in the UK [53], the Brandenburg University of Technology Cottbus-Senftenberg in Germany [10], DLR Braunschweig's Aeroacoustic Wind Tunnel (AWB) in Germany [50], Friedrich-Alexander-Universität Erlangen-Nürnberg in Germany, Florida State University in the USA, the Institute of Sound and Vibration Research (ISVR) of the University of Southampton in UK [28], the University of Siegen in Germany and Virginia Polytechnic Institute and State University (Virginia Tech) in the USA [40]. An important consideration about

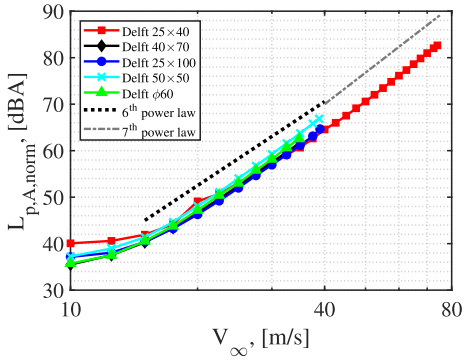

Fig. 14. Overall A-weighted $L_{p,A}$ background noise levels for different flow velocities for the five nozzles available at the A-tunnel. The values are normalized using Eq. (1).

Table 3
Characteristics of the different nozzles available in the A-tunnel.

Name	Area [m^2]	V_{max} [m/s]	$L_{p,A}$ at 30 m/s [dBA]	k
Delft 25 × 40	0.1	74	47.7	6.89
Delft 40 × 70	0.28	35	52	6.23
Delft 25 × 100	0.25	40	50.9	6.28
Delft 50 × 50	0.25	38.8	53.2	6.57
Delft ϕ60	0.28	35	52.7	6.39

Table 4
Characteristics of other open-jet aeroacoustic wind tunnels and their respective nozzles from universities and research institutions (first rows) and industry (last rows), as reported in the literature. Extracted from Refs. [10,16,28,40,49–55].

Name	Dimensions [m]	Area [m^2]	V_{max} [m/s]	θ [deg]	k
Adeilaide	0.275 × 0.075	0.02	40	90	4.22
Beihang	1 × 1	1	80	90	5.84
Bristol	0.2 × 0.6	0.12	70	90	5.79
Cottbus	Diameter 0.2	0.03	50	90	7.6
DLR	1.2 × 0.8	0.96	65	72	6.82
Erlangen	0.2 × 0.233	0.05	45	45	6.35
Florida	1.12 × 0.74	0.83	42	65	6.57
ISVR	0.45 × 0.15	0.07	95	90	6.8
Siegen	0.133 × 0.133	0.02	30	90	3.81
Virginia	1.83 × 1.83	3.35	75	–	–
Audi	3.94 × 2.8	11	83	52	6.63
BMW	–	10	50	69	6.13
Daimler	6.9 × 4.03	27.8	71	32	6.36
DNW	8 × 6	48	80	90	–
DTF	5.56 × 3.34	18.57	53	40	5.3
Ford	–	20	52	49	5.13
Hyundai	7 × 4	28	55	29	6.09
IVK	5.8 × 3.87	22.46	73	50	6.54
Nissan	7 × 4	28	52	–	5.79
Pininfarina	Semicircle $\phi = 5.64$ m	11.75	70	50	6.85
Porsche	6.2 × 3.6	22.32	83	90	6.38

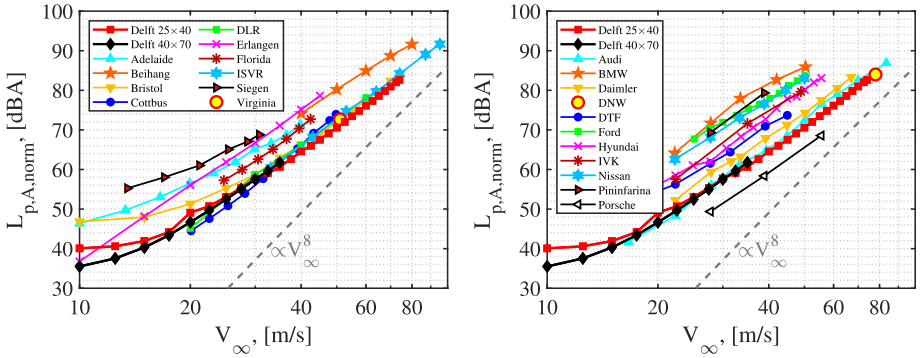

Fig. 15. Comparison of the overall A-weighted $L_{p,A}$ background noise levels for different flow velocities with other aeroacoustic wind tunnels of (a) universities and research institutions and (b) industry. The values are normalized using Eq. (1). Data extracted from Refs. [10,16,28,40,49–55].

the stability wind tunnel of Virginia Tech is that it is not an open-jet wind tunnel, but rather an *hybrid* wind tunnel equipped with Kevlar walls that allow for a closed test section from the aerodynamic point of view, while being almost acoustically transparent to the sound waves, allowing for acoustic measurements outside of the flow. Thus, the noise sources of this tunnel have, most likely, a different origin than the rest of wind tunnels listed here.

In Fig. 15a it is observed that the two nozzles of the A-tunnel considered (Delft 25 × 40 and Delft 40 × 70) compare relatively well with the rest of the wind tunnels of university and research institutions in terms of background noise. They even provide one of the lowest background noise levels at some velocities, followed closely by Cottbus, Bristol, DLR, ISVR and Virginia Tech. Interestingly, Cottbus, DLR and ISVR present the values of the exponent k closest to 8: 7.6, 6.82, and 6.8, respectively. The 8th power law with the flow velocity has been plotted in Fig. 15a and b as an indication.

The industrial wind tunnels selected for the current comparison were (in alphabetic order): the Audi AG aeroacoustic wind tunnel (AAWK) in Germany [49], the aeroacoustic wind tunnel of BMW Technik AG in Germany, the DaimlerChrysler AG Aeroacoustic wind tunnel (AAWT) in USA, the Large Low-Speed Facility (LLF) of the German–Dutch Wind Tunnels (Stichting DNW), in the Netherlands [47,55], the Driveability Test Facility Wind Tunnel No. 8 (DTF-WT8) in USA, the Ford of Europe AG aeroacoustic wind tunnel in Germany, the Hyundai Motor Company Full-Scale Aeroacoustic Wind Tunnel (HAWT) in South Korea, the Institut für Verbrennungsmotoren und Kraftfahrwesen (IVK) aeroacoustic wind tunnel of Stuttgart University in Germany[1], the Low-Noise Full-Scale Wind Tunnel of Nissan Motor Co. Ltd. in Japan, the Pininfarina S.p.A. wind tunnel in Italy [54], and the aeroacoustic wind tunnel of Porsche AG in Germany [51].

The performance of the two nozzles of the A-tunnel can be compared to the industrial wind tunnels in Fig. 15b. Once again, they provide some of the lowest background noise levels, presenting a very similar behavior as the wind tunnel of Audi AG. Only the results of the aeroacoustic wind tunnel of Porsche AG are about 6 dBA lower than those of the A-tunnel. In terms of the power-law exponent k, the industrial wind tunnels present values between 5.1 (Ford Europe AG) and 6.9 (Pininfarina S.p.A.).

Even though the background noise levels are normalized with respect to the nozzle area and the distance to the observer using Eq. (1), it should be kept in mind that the maximum Reynolds

[1] Despite being located at a university, the IVK wind tunnel was considered as an industrial wind tunnel, given its main use and dimensions.

number achievable in these wind-tunnel facilities greatly depends on the nozzle exit area (as well as the maximum velocity achievable V_{max}). The facilities considered in the comparisons of Fig. 15 have considerably different sizes. For example, the Delft 40×70 nozzle has a nozzle exit area about 14 times larger than the smallest wind tunnels (University of Adelaide and University of Siegen), but about 170 times smaller than the largest wind tunnel (DNW-LLF).

5.2. Free-field propagation assessment

One of the most important features of an anechoic room is the region of space where the inverse square law spreading [45] holds, i.e. where the free-field sound propagation conditions are present [26] without significant reflections of the walls, floor or ceiling. The expected sound pressure level L_p at a distance r from the observer in the free field can be calculated using the following expression [45], which considers omnidirectional spherical spreading of sound

$$L_p(r) = L_p(r_0) - 20\log\left(\frac{r}{r_0}\right), \tag{3}$$

where r_0 is a reference distance to the source, normally considered as 1 m. The atmospheric absorption of sound is neglected in this equation due to the relatively small distances considered.

The measured deviation from the expected free-field decay ΔL_p can be calculated for every distance r using the following equation

$$\Delta L_p = L_{p,exp} - L_{p,ref}, \tag{4}$$

where $L_{p,exp}$ and $L_{p,ref}$ are the measured and modeled sound pressure levels (calculated using Eq. (3)), respectively.

The maximum allowable ΔL_p values per third-octave frequency band for an anechoic room are given by the standards in ISO3745 [56], see Table 5.

In order to assess the free-field conditions a simple setup, following the guidelines in the ISO3745 [26,56], was used consisting of:

- A sound source, namely a *Visaton K50 SQ* speaker [57], situated 0.5 m over the wind-tunnel nozzle to simulate a representative experimental setup. This speaker emitted the same broadband white noise signal for each measurement during 60 s.
- A reference *G.R.A.S. 40PH* microphone [34] next to the speaker ensured the repeatability of the measurements.
- A second *G.R.A.S. 40PH* microphone [34] mounted on a guide wire. For each measurement, the microphone was displaced 0.1 m away from the sound source, starting from an initial distance of 1 m until a distance of 2 m. The direction selected was the one pointing at the position where the microphone array is normally placed for aeroacoustic experiments. Other directions were considered and showed almost identical results but are not presented here for the sake of brevity.

The measured ΔL_p values for each third-octave frequency band with respect to the distance to the source r are presented in Fig. 16.

Table 5
Maximum allowable difference between measured and modeled free-field L_p for an anechoic room depending on the frequency range according to the standards in ISO3745 [56].

One-third-octave-band center frequency f [Hz]	Allowable ΔL_p [dB]
$f \leqslant 630$	± 1.5
$800 \leqslant f \leqslant 5000$	± 1
$f \geqslant 6300$	± 1.5

The maximum allowable differences from Table 5 are plotted as red dash-dotted lines. It can be observed that all the frequency bands above 250 Hz fulfill the standards in ISO3745 [56] for the full range of distances considered. The results for the three next one-third-octave bands below 250 Hz, (125 Hz, 160 Hz and 200 Hz) only show acceptable values up to $r = 1.5$ m. For aeroacoustic experiments, the distance between the microphone array and the jet axis normally corresponds to $r \leqslant 1.5$ m, so acoustic measurements at these three frequency bands could be considered as acceptable in that distance range. These results are consistent with the expected cutoff frequency of 173.5 Hz mentioned in Section 2.

5.3. Reverberation time

The reverberation time (T_{60}) [45] of a room is typically defined as the amount of time it takes for the sound pressure level (L_p) of the received signal to decrease by 60 dB, measured after the generated test signal is abruptly ended. In the current study, a clapper device for acoustic measurements [58] was used to produce a loud ($L_p \approx 85$ dB) broadband, impulse signal, which was recorded by a single reference *G.R.A.S. 40PH* microphone at the array, which was placed 1 m away from the jet axis. A total of four measurements were performed placing the clapper device on top of the nozzle of the wind tunnel, in order to obtain results that are representative for the expected experimental setups. An average T_{60} value of 0.22 s was measured, which corresponds to the anechoic or *acoustically dead* category according to the ISO norm 3382 [59]. It should be noted that, during these experiments, the exit of the wind-tunnel nozzle was kept open to better represent the actual conditions during real testing. For purely acoustic measurement not requiring flow, it is recommended to cover the nozzle to minimize the reverberation originating from the settling chamber and the rest of the wind-tunnel circuit.

5.4. Point spread function (PSF)

In order to assess the overall performance of the phased microphone array and the anechoic chamber around the test section and confirm that there are no sound reflections, the point spread function (PSF) of the array was evaluated. This term refers to the array response to the presence of a point sound source at a certain frequency, typically using conventional frequency domain beamforming [44]. An omnidirectional sound source was located in the jet axis 0.5 m above the nozzle exit plane, in order to represent a typical position of a test model in the wind tunnel. The source is a customized miniature sound source type *QindW* developed by Qsources [60]. It has an oblong shape with a length of 110 mm and a diameter of 20 mm. The source sound power is omnidirectional in the azimuthal plane and has a flat frequency response from approximately 500 Hz to 6300 Hz when emitting white noise [61]. The source was aligned with the center of the microphone array, i.e. it had the coordinates $(X, Y, Z) = (0.5, 0, 0)$ m using the system of reference defined in Fig. 5a. The microphone array had the distribution shown in Fig. 7b and the array plane was placed 1 m away from the source in the negative Y direction parallel to the XZ plane.

Fig. 17 depicts the conventional frequency domain beamforming PSF obtained experimentally (Fig. 17a) compared with the simulated PSF for the same microphone array distribution and source location (Fig. 17b) for a one-third-octave band centered at 2 kHz. The main lobe is slightly elongated in the Z direction because of the smaller size of the microphone array in that direction. It can be observed that the differences between both source plots are relatively small, as desired. The theoretical PSF presents a slightly narrower main lobe and slightly lower sidelobes than the experimental one, as

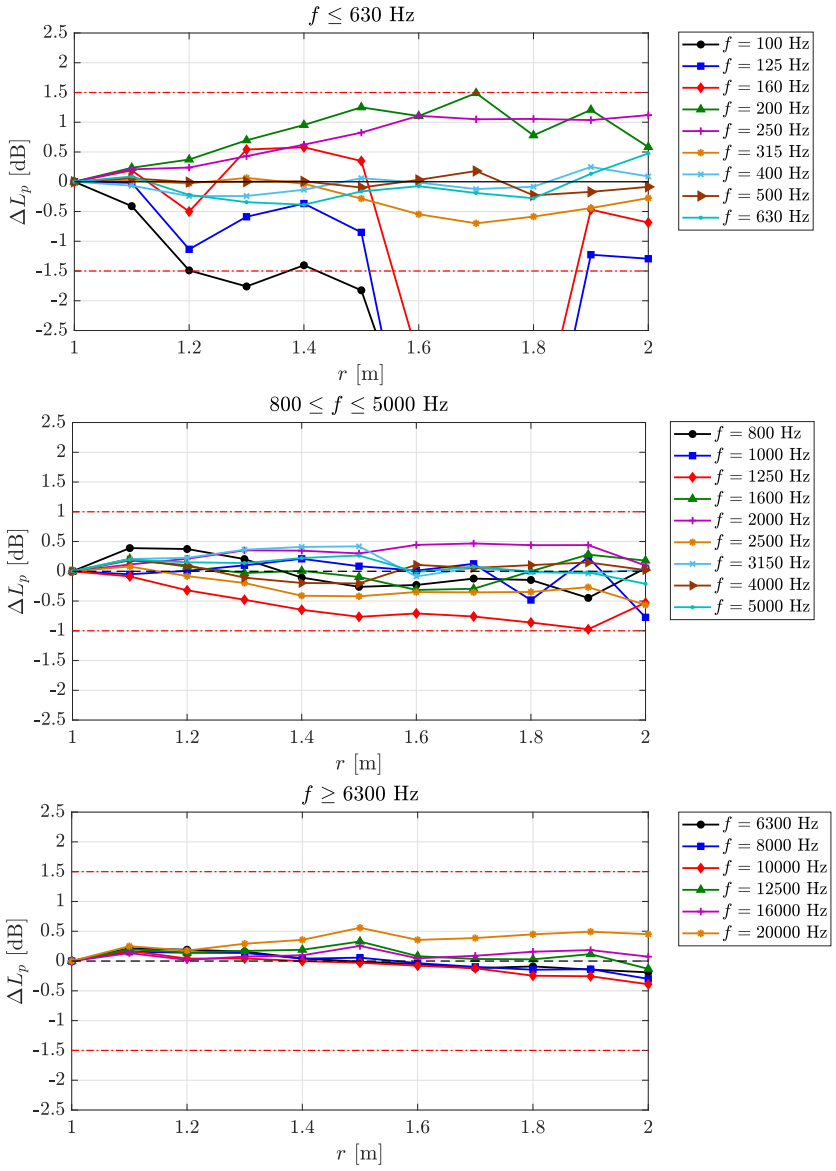

Fig. 16. Deviation from the free-field decay with respect to the distance to the source r. The tolerances according to ISO3745 [56] are depicted as dashed red lines. (For interpretation of the references to color in this figure legend, the reader is referred to the web version of this article.)

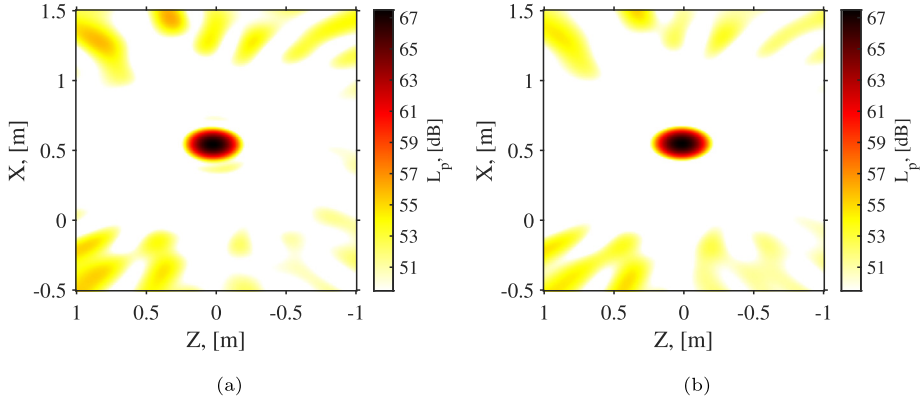

Fig. 17. (a) Experimental and (b) simulated array PSF for a source located at $(X, Y, Z) = (0.5, 0, 0)$ m for a one-third-octave band centered at 2 kHz.

expected. This is mostly explained by the fact that the source used is not a point source (like in the simulations) or perfectly omnidirectional. In addition, the response and accuracy of the positioning of the microphones are also not perfect. Overall, no physical sound source is observed in the dynamic range selected (18 dB), and the sidelobe pattern found in the experimental PSF is almost identical

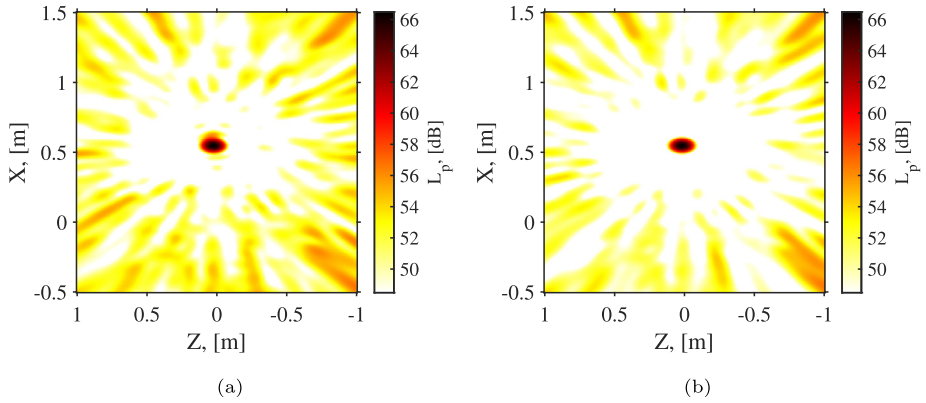

Fig. 18. (a) Experimental and (b) simulated array PSF for a source located at $(X, Y, Z) = (0.5, 0, 0)$ m for a one-third-octave band centered at 4 kHz.

to the theoretical one. The effect of these sidelobes in the measurements can be reduced by using advanced acoustic imaging algorithms [62,63].

Comparable results are obtained for the case of a one-third-octave band centered at 4 kHz, see Fig. 18. The main lobe is narrower and there is a higher presence of sidelobes compared to Fig. 17, as expected due to the higher frequency [44,63]. Once again, no relevant background noise sources are observed for these dynamic and frequency range. Other frequencies showed similar results but are not shown here for brevity.

6. Conclusion

This paper explains the design and performance of the recently-refurbished aeroacoustic wind tunnel of Delft University of Technology (A-tunnel). This facility is a vertical wind tunnel with an anechoic plenum around the test section (with a cutoff frequency of 200 Hz) and it allows for the use of interchangeable nozzles. This facility is mainly meant for aeroacoustic measurements, fundamental studies in laminar-turbulent transition and flow control. Therefore, it is equipped with a re-configurable microphone array for acoustic imaging, and devices for flow characterization, such as a Pitot probe, and HWA and PIV systems. Overall, the A-tunnel has shown a satisfactory performance both in the flow characterization (in terms of flow uniformity and turbulence intensity) and in the acoustic characterization (in terms of background noise levels, free-field propagation and reverberation time), compared to other aeroacoustic wind-tunnel facilities from literature.

To this date, this facility has been primarily employed for the study of airfoil trailing-edge noise [64], the performance of noise-reduction devices [48,65], as well as the noise emissions from small-sized propellers [61].

Declaration of Competing Interest

The authors declare that they have no known competing financial interests or personal relationships that could have appeared to influence the work reported in this paper.

Acknowledgements

The authors would like to thank Christian H.C. Vlemmix for his help and support for designing and assembling the microphone array structure and the preliminary characterization tests in the A-tunnel, and Henk-Jan Siemer for his support throughout the whole project.

References

[1] Mueller T. Aeroacoustic measurements. Springer Science & Business Media, Berlin, Germany; 2002, ISBN: 978-3-642-07514-8. URL:https://books.google.com/books?hl=en&lr=&id=MU6WLXFJLWgC&pgis=1.
[2] Kotsonis M, Ghaemi S, Veldhuis L, Scarano F. Measurement of the body force field of plasma actuator. J Appl Phys D Appl Phys 44 (4):2011. doi: 10.1088/0022-3727/44/4/045204. URL: https://doi.org/10.1088/0022-3727/44/4/045204.
[3] Owen B, Lee DS, Lim L. Flying into the future: aviation emission scenarios to 2050. Environ Sci Technol Am Chem Soc 2010;44:2255–60. https://doi.org/10.1021/es902530z. URL:https://pubs.acs.org/doi/pdf/10.1021/es902530z.
[4] Merino-Martinez R, Bertsch L, Snellen M, Simons DG. Analysis of landing gear noise during approach. In: 22nd AIAA/CEAS aeroacoustics conference, May 30 – June 1 2016, Lyon, France, 2016, AIAA paper 2016-2769. doi: 10.2514/6.2016-2769. URL:http://arc.aiaa.org/doi/pdf/10.2514/6.2016-2769.
[5] Arce León C, Merino-Martinez R, Ragni D, Avallone F, Snellen M. Boundary layer characterization and acoustic measurements of flow–aligned trailing edge serrations. Exp Fluids 2016;57(182):1–22. https://doi.org/10.1007/s00348-016-2272-z. URL:http://link.springer.com/10.1007/s00348-016-2272-z.
[6] Oerlemans S. Reduction of wind turbine noise using blade trailing edge devices. In: 22nd AIAA/CEAS aeroacoustics conference, May 30 – June 1 2016, Lyon, France, 2016, AIAA paper 2016-3018. doi: 10.2514/6.2016-3018. URL: http://arc.aiaa.org/doi/pdf/10.2514/6.2016-3018.
[7] Lockard DP, Humphreys WM, Khorrami MR, Fares E, Casalino D, Ravetta PA. Comparison of computational and experimental microphone array results for an 18% – scale aircraft model. Int J Aeroacoust 16(4–5):2017;358–81, SAGE Publications Ltd., London, United Kingdom. doi: 10.1177/1475472X17718724. URL:http://journals.sagepub.com/doi/full/10.1177/1475472X17718724.
[8] Avallone F, van der Velden WCP, Ragni D. Benefits of curved serrations on broadband trailing–edge noise reduction. J Sound Vib 2017;400:167–77. https://doi.org/10.1016/j.jsv.2017.04.007. URL: https://doi.org/10.1016/j.jsv.2017.04.007.
[9] Avallone F, van der Velden WCP, Ragni D, Casalino D. Noise reduction mechanisms of sawtooth and combed–sawtooth trailing–edge serrations. J Fluid Mech 2018;848:560–91. https://doi.org/10.1017/jfm.2018.377. URL: https://doi.org/10.1017/jfm.2018.377.
[10] Sarradj E, Fritzsche C, Geyer T, Giesler J. Acoustic and aerodynamic design and characterization of a small-scale aeroacoustic wind tunnel. Appl Acoust 2009;70:1073–80. https://doi.org/10.1016/j.apacoust.2009.02.009. URL: https://doi.org/10.1016/j.apacoust.2009.02.009.
[11] Khorrami MR, Fares E. Toward noise certification during design: airframe noise simulations for full-scale, complete aircraft. CEAS Aeronaut J 2019;10:31–67. https://doi.org/10.1007/s13272-019-00378-1. URL: https://doi.org/10.1007/s13272-019-00378-1.
[12] Stoker R, Guo Y, Streett C, Burnside N. Airframe noise source locations of a 777 aircraft in flight and comparisons with past model-scale tests. In: 9th AIAA/CEAS aeroacoustics conference, May 12–14 2003, Hilton Head, South California, USA, 2003, AIAA paper 2003-3232. doi: 10.2514/6.2003-3232. URL: http://arc.aiaa.org/doi/pdf/10.2514/6.2003-3232.
[13] Shaw R. The influence of hole dimensions on static pressure measurements. J Fluid Mech 1960;7(4):550–64. https://doi.org/10.1017/S0022112060000281. URL:https://www.cambridge.org/core/journals/journal-of-fluid-mechanics/article/influence-of-hole-dimensions-on-static-pressure-measurements/6FD2B81E5DBA40093D1B9E725F9B107B.
[14] Pagani CCJ, Souza DS, Medeiros MAF. Slat noise: aeroacoustic beamforming in closed-section wind tunnel with numerical comparison. AIAA J 2016;54(7):2100–15. https://doi.org/10.2514/1.J054042. URL: http://arc.aiaa.org/doi/abs/10.2514/1.J054042.
[15] VanDercreek CP, Merino-Martinez R, Snellen M, Simons DG. Comparison of cavity geometries for a microphone array in a open-jet wind-tunnel experiment. In: 8th Berlin beamforming conference, March 2–3 2020, Berlin, Germany, GFaI, e.V., Berlin, 2020, BeBeC-2020-D7. URL:http://www.bebec.eu/Downloads/BeBeC2020/Papers/BeBeC-2020-D07.pdf.

[16] Duell E, Walter J, Arnette S, Y J. Recent advances in large-scale aeroacoustic wind tunnels. In: 8th AIAA/CEAS aeroacoustics conference, 17–19 June 2002, Breckenridge Co, USA, 2002, AIAA paper 2002–2503. doi: 10.2514/6.2002-2503. URL: http://arc.aiaa.org/doi/abs/10.2514/6.2002-2503.

[17] Guidati S, Brauer C, Wagner S. The reflection canceller – phased array measurements in a reverberating environment. In: 8th AIAA/CEAS Aeroacoustics Conference and Exhibit, June 17–19, 2002, Breckenridge, Colorado, USA, 2002, AIAA paper 2002-2462. doi: 10.2514/6.2002-2462. URL: https://arc.aiaa.org/doi/pdf/10.2514/6.2002-2462.

[18] Sijtsma P, Holthusen H. Corrections for mirror sources in phased array processing techniques. In: 9th AIAA/CEAS aeroacoustics conference, May 12–14, 2003, Hilton Head, South Carolina, USA, 2003, AIAA paper 2003-3196. doi: 10.2514/6.2003-3196. URL: https://arc.aiaa.org/doi/abs/10.2514/6.2003-3196.

[19] Pereira Gomes J, Bergmann A, Holthusen H. Aeroacoustic wind tunnel design (part of the Aircraft Noise Generation and Assessment special issue), CEAS Aeronaut J 10(1):2019;231–49. doi: 10.1007/s13272-019-00372-7. URL: https://link.springer.com/article/10.1007/s13272-019-00372-7.

[20] Anderson JDJ. Fundamentals of aerodynamics, 3rd ed., McGraw–Hill Series in Aeronautical and Aerospace Engineering, 2001, ISBN: 0-07-237335-0. URL: https://avionicsengineering.files.wordpress.com/2016/11/john-d-anderson-jr-fundamentals-of-aerodynamics.pdf.

[21] Amiet RK. Correction of open jet wind tunnel measurements for shear layer refraction. In: 2nd AIAA aeroacoustics conference, March 24 – 26, Hampton, VA, USA, 1975, AIAA paper 1975-532. doi: 10.2514/6.1975-532. URL: http://arc.aiaa.org/doi/pdf/10.2514/6.1975-532.

[22] Amiet RK. Refraction of sound by a shear layer. J Sound Vib 1978;58 (4):467–82. https://doi.org/10.1016/0022-460X(78)90353-X. URL: https://doi.org/10.1016/0022-460X(78)90353-X.

[23] Ernst D, Spehr C, Berkefeld T. Decorrelation of acoustic wave propagation through the shear layer in open jet wind tunnel. In: 21st AIAA/CEAS aeroacoustics conference, June 22–26 2015, Dallas, TX, USA, 2015, AIAA paper 2015-2976. doi: 10.2514/6.2015-2976. URL: https://doi.org/10.2514/6.2015-2976.

[24] Sijtsma P, Oerlemans S, Tibbe T, Berkefeld T, Spehr C. Spectral broadening by shear layers of open jet wind tunnels. In: 20th AIAA/CEAS Aeroacoustics Conference, June 16–20 2014, Atlanta, GA, USA, 2014, AIAA paper 2014-3178. doi: 10.2514/6.2014-3178. URL: https://doi.org/10.2514/6.2014-3178.

[25] Tester BJ, Sijtsma P. Measurement and analysis of phased array data on haystacked tones from a source located in a free jet. In: 23rd AIAA/CEAS aeroacoustics conference, June 5–9 2017, Denver, Colorado, USA, 2017, AIAA paper 2017-3864. doi: 10.2514/6.2017-3864. URL: http://arc.aiaa.org/doi/pdf/10.2514/6.2017-3864.

[26] Kopiev V, Palchikovskiy V, Bersenev Y, Makashov S, Belyaev I, Korin I, et al. Design and quantification of an anechoic facility in PNRPU. Procedia Eng 2017;176:264–72. https://doi.org/10.1016/j.proeng.2017.02.314. URL: https://doi.org/10.1016/j.proeng.2017.02.314.

[27] de Santana LD, Carmo M, Catalano FM. The update of an aerodynamic wind-tunnel for aeroacoustics testing. J Aerosp Technol Manage 2014;6(2):111–8. https://doi.org/10.5028/jatm.v6i2.308. URL: https://asa.scitation.org/doi/abs/10.5028/jatm.v6i2.308.

[28] Chong TP, Joseph PF, Davies POAL. Design and performance of an open jet wind tunnel for aero-acoustic measurement. Appl Acoust 2009;70:605–14. https://doi.org/10.1016/j.apacoust.2008.06.011. URL: https://doi.org/10.1016/j.apacoust.2008.06.011.

[29] Arce León C, Merino-Martinez R, Ragni D, Avallone F, Scarano F, Pröbsting S, et al. Effect of trailing edge serration-flow misalignment on airfoil noise emission. J Sound Vib 405:2017;19–33. doi: 10.1016/j.jsv.2017.05.035. URL: https://doi.org/10.1016/j.jsv.2017.05.035.

[30] Yarusevych S, Kotsonis M. Steady and transient response of a laminar separation bubble to controlled disturbances. J Fluid Mech 2017;813:955–90. https://doi.org/10.1017/jfm.2016.848. URL:https://www.cambridge.org/core/journals/journal-of-fluid-mechanics/article/steady-and-transient-response-of-a-laminar-separation-bubble-to-controlled-disturbances/4E93B399FB058661412628A80BB1E52E.

[31] Morel T. Design of two-dimensional wind tunnel contractions. J Fluids Eng 1977;99(2):371–7. https://doi.org/10.1115/1.3448764. URL: https://doi.org/10.1115/1.3448764.

[32] Flamex Basic – Acoustic Absorbing Foam. URL:https://www.merford.com/media/202626/flamex-basic.pdf [accessed in March 2017].

[33] Rusz R. Design of a fully anechoic chamber. Master's thesis, Kungliga Tekniska Högskolan (KTH), Brinellvägen 8, 114 28 Stockholm, Sweden, TRITA-AVE 2015:36. ISSN: 1651-7660; 2015. URL:http://www.diva-portal.org/smash/get/diva2:893785/FULLTEXT01.pdf.

[34] G.R.A.S. Sound & Vibration – 40PH CCP Free–field array microphone. URL: http://www.gras.dk/products/special-microphone/array-microphones/product/178-40ph [accessed in March 2017].

[35] G.R.A.S. Sound & Vibration – 42AA Pistonphone class 1. URL:https://www.gras.dk/products/calibration-equipment/reference-calibrator/product/255-42aa [accessed in March 2017].

[36] G.R.A.S. Sound & Vibration – AA0028 10 m SMB – BNC cable. URL:https://www.gras.dk/products/cables/product/418-aa0028-extension-cable-for-array-microphones-smb-female-to-bnc [accessed in March 2017].

[37] Vlemmix CHC. Acoustic Array Design – The design of a reconfigurable phased microphone array for aeroacoustic wind tunnel measurements. Master's thesis, Delft University of Technology (December 2017). URL:https://repository.tudelft.nl/islandora/object/uuid%3Adb51ea64-71b1-446d-9022-61842f2e794a.

[38] Luesutthiviboon S, Malgoezar AMN, Merino-Martinez R, Snellen M, Sijtsma P, Simons DG. Enhanced HR-CLEAN-SC for resolving multiple closely spaced sound sources. Int J Aeroacoust 2019;18(4–5):392–413. https://doi.org/10.1177/1475472X19852938. URL: https://doi.org/10.1177/1475472X19852938.

[39] Findanis N, Ahmed N. Wind tunnel concept of proof investigations in the development of novel fluid mechanical methodologies and devices. Wind tunnels and experimental fluid dynamics research; 2011. ISBN: 978-0-128-09651-2. doi: 10.5772/18798. URL:https://www.intechopen.com/books/wind-tunnels-and-experimental-fluid-dynamics-research/wind-tunnel-concept-of-proof-investigations-in-the-development-of-novel-fluid-mechanical-methodologi.

[40] Remillieux MC, Crede ED, Camargo HE, Burdisso RA, DW J, Rasnick M, van Seeters P, et al. Calibration and demonstration of the new virginia tech anechoic wind tunnel. In: 14th AIAA/CEAS aeroacoustics conference (29th AIAA Aeroacoustics Conference), May 5–7, 2008, Vancouver, British Columbia, Canada, 2008, AIAA paper 2008-2911. doi: 10.2514/6.2008-2911. URL: http://arc.aiaa.org/doi/pdf/10.2514/6.2008-2911.

[41] Pascioni K, Reger R, Edstrand A, Cattafesta III LN. Characterization of an aeroacoustic wind tunnel facility. In: 43rd International congress and exposition of noise control engineering, 16–19 November, 2014, Melbourne, Australia, 2014. URL:https://www.acoustics.asn.au/conference_proceedings/INTERNOISE2014/papers/p584.pdf.

[42] Tourn S, Pallarès J, Cuesta I, Schmidt Paulsen U. Characterization of a new open jet wind tunnel to optimize and test vertical axis wind turbines. J Renew Sustain Energy 9(033302):2017;1–14. doi: 10.1063/1.4982750. URL: https://doi.org/10.1063/1.4982750.

[43] Welch PD. The use of fast fourier transform for the estimation of power spectra: a method based on time averaging over short, modified periodograms. IEEE Trans Audio Electroacoust AU-15(2):1967;70–73. doi: 10.1109/TAU.1967.1161901. URL:http://ieeexplore.ieee.org/stamp/stamp.jsp?arnumber=1161901.

[44] Merino-Martinez R. Microphone arrays for imaging of aerospace noise sources, .Ph.D. thesis, Delft University of Technology, ISBN: 978-94-028-1301-2; 2018. doi: 10.4233/uuid:a3231ea9-1380-44f4-9a93-dbbd9a26f1d6. URL:https://repository.tudelft.nl/islandora/object/uuid:a3231ea9-1380-44f4-9a93-dbbd9a26f1d6?collection=research.

[45] Rossing TD. Handbook of acoustics. 2nd ed., Springer Science & Business Media, New York, USA; 2007, ISBN: 987-0-387-30446-5. URL: https://books.google.nl/books/about/Springer_Handbook_of_Acoustics.html?id=4ktVwGe_dSMC&redir_esc=y.

[46] Lighthill MJ. On sound generated aerodynamically, I: General theory. Proc R Soc Lond Ser A Math Phys Sci 211(1107):1952;564–87. doi: 10.1098/rspa.1952.0060. URL: https://doi.org/10.1098/rspa.1952.0060.

[47] Holthusen H, Bergmann A, Sijtsma P. Investigations and measures to improve the acoustic characteristics of the German-Dutch Wind Tunnel DNW–LLF. In: 18th AIAA/CEAS aeroacoustics conference, 4–6 June 2012, Colorado Springs, USA, 2012, AIAA paper 2012-2176. doi: 10.2514/6.2012-2276. URL: http://arc.aiaa.org/doi/pdf/10.2514/6.2012-2176.

[48] Rubio Carpio A, Merino-Martinez R, Avallone F, Ragni D, Snellen M, van der Zwaag S. Experimental characterization of the turbulent boundary layer over a porous trailing edge for noise abatement. J Sound Vib 443:2019:537–58. doi: 10.1016/j.jsv.2018.12.010. URL: https://doi.org/10.1016/j.jsv.2018.12.010.

[49] Wickern G, Lindener N. The audi aeroacoustic wind tunnel: final design and first operational experience. Tech. Rep. 2000-01-0868, Society of Automotive Engineers, Inc. (SAE) - Committee on Aircraft Noise (SAE A-21), 400 Commonwealth Drive, Warrendale, PA 15096 (January 2000). doi: 10.4271/2000-01-0868. URL: https://doi.org/10.4271/2000-01-0868.

[50] Pott-Pollenske M, Delfs J. Enhanced capabilities of the aeroacoustic wind tunnel Braunschweig. In: 14th AIAA/CEAS Aeroacoustics Conference (29th AIAA Aeroacoustics Conference), May 5–7, 2008, Vancouver, British Columbia, Canada, 2008, AIAA paper 2008-2910. doi: 10.2514/6.2008-2910. URL: http://arc.aiaa.org/doi/pdf/10.2514/6.2008-2910.

[51] Stumpf H, Röser P, Wiegand T, Pfäfflin B, Ocker J, Müller R, et al. The new aerodynamic and aeroacoustic wind tunnel of the Porsche AG. In: 15th Internationales Stuttgarter Symposium, Springer Vieweg, Wiesbaden.; 2015. p. 811–26. doi: 10.1007/978-3-658-08844-6_54. URL: https://doi.org/10.1007/978-3-658-08844-6_54.

[52] Liu P, Xing Y, Guo H, Li L. Design and performance of a small-scale aeroacoustic wind tunnel. Appl Acoust 2017;116:65–9. https://doi.org/10.1016/j.apacoust.2016.09.014. URL: https://doi.org/10.1016/j.apacoust.2016.09.014.

[53] Mayer Y, Jawahar HK, Szőke M, Ali SAS, Azarpeyvand M. Design and performance of an aeroacosutic wind tunnel facility at the University of Bristol. Appl Acoust 2019;155:358–70. https://doi.org/10.1016/j.apacoust.2019.06.005. URL: https://doi.org/10.1016/j.apacoust.2019.06.005.

[54] Pininfarina website. URL:https://pininfarina.it/en/wind-tunnel/ [accessed in November 2019].

[55] DNW-LLF website. URL:https://www.dnw.aero/media-center/downloads/brochures//download/5 [accessed in November 2019].

[56] ISO norm 3745 – Acoustics – Determination of sound power levels and sound energy levels of noise sources using sound pressure – Precision methods for anechoic rooms and hemi-anechoic rooms, Tech. Rep. 3, International Organization for Standardization; 2012. URL:https://www.iso.org/standard/45362.html.

[57] Visaton – Speaker K 50 SQ – 8 Ohm. URL:http://www.visaton.de/en/products/fullrange-systems/k-50-sq-8-ohm [accessed in March 2017].
[58] Eurofysica – Clapper for acoustic measurements, https://www.eurofysica.nl/webshop/natuurkunde/golven-licht-geluid/geluid/product/klapper-voor-geluidsmeting-1, accessed in March 2017. URL:https://www.eurofysica.nl/webshop/natuurkunde/golven-licht-geluid/geluid/product/klapper-voor-geluidsmeting-1.
[59] ISO norm 3382 – Acoustics – Measurement of room acoustic parameters. Tech. Rep. 1, International Organization for Standardization; 2012. URL:https://www.iso.org/standard/46520.html.
[60] Qsources website. URL:https://www.qsources.be/ [accessed in November 2019].
[61] Vieira A, Snellen M, Malgoezar AMN, Merino-Martinez R, Simons DG. Analysis of shielding of propeller noise using beamforming and predictions. J Acoust Soc Am 2019;146(2):1085–98. https://doi.org/10.1121/1.5121398. URL: https://doi.org/10.1121/1.5121398.
[62] Merino-Martinez R, Snellen M, Simons DG. Functional beamforming applied to imaging of flyover noise on landing aircraft. J Aircraft 2016;53(6):1830–43. https://doi.org/10.2514/1.C033691. URL: http://arc.aiaa.org/doi/abs/10.2514/1.C033691.
[63] Merino-Martinez R, Sijtsma P, Snellen M, Ahlefeldt T, Antoni J, Bahr CJ, et al. A review of acoustic imaging methods using phased microphone arrays (part of the Aircraft Noise Generation and Assessment special issue). CEAS Aeronaut J 2019;10(1):197–230. https://doi.org/10.1007/s13272-019-00383-4. URL: https://rdcu.be/brsL2.
[64] Merino-Martinez R, Luesutthiviboon S, Zamponi R, Rubio Carpio A, Ragni D, Sijtsma P, et al. Assessment of the accuracy of microphone array methods for aeroacoustic measurements. J Sound Vib 470(115176):2020;1–24. doi: 10.1016/j.jsv.2020.115176. URL: https://doi.org/10.1016/j.jsv.2020.115176.
[65] Rubio Carpio A, Merino-Martinez R, Avallone F, Ragni D, Snellen M, van der Zwaag S. Broadband trailing edge noise reduction using permeable metal foams. In: 46th International congress and exposition of noise control engineering, 27–30 August, 2017, Hong Kong, International Institute of Noise Control Engineering (I-INCE), 2017. URL:https://repository.tudelft.nl/islandora/object/uuid%3Aedae7923-d41c-4169-ae9d-65a8e02eb583?collection=research47.